Mine Water and the Environment (2021) 40:1048–1060
https://doi.org/10.1007/s10230-021-00826-7

TECHNICAL ARTICLE

CFD-DEM Coupled Simulation of Broken Rock Mass Movement During Water Seepage in an Underground Goaf Reservoir

Cun Zhang[1,2,3] · Sheng Jia[2] · Qingsheng Bai[4] · Hongwei Zhang[2] · Yanhong Chen[2] · Yue Jiao[2]

Received: 15 December 2020 / Accepted: 11 September 2021 / Published online: 21 September 2021
© Springer-Verlag GmbH Germany, part of Springer Nature 2021

Abstract

Underground water reservoir (UWR) technology has been used to protect mine water resources. The main underground space for UWRs is the caving zone formed by longwall mining. Broken rock mass movement in the caving zone affects the porosity distribution and seepage characteristics during the UWR's circulation, storage, and discharge. We used a fluid-solid coupled model, implemented in PFC3D and combined with Python, to simulate water seepage in the caving zone. The influence of particle size and fluid element size on the error of the simulation results was analysed. Then, we investigated the effect of seepage on broken rock mass porosity under different stress states. Simulations with various particle sizes and compaction stresses show that the average displacement of broken rock decreases exponentially with increased stress. Because large broken particles form the primary bearing structure in the model, it is mostly small particles that move under high-stress levels, so porosity is less affected. Larger particles also migrate if the compaction stress is low; this significantly changes the porosity and leads to roof uplift. Finally, we designed an engineering scale model based on our simulation method using the actual UWR situation in a coal mine.

Keywords Underground mine reservoir · Caving zone · Particle size · Compaction stress · Porosity

Introduction

In recent years, coal production in China has gradually shifted from the eastern coal fields to the west. However, the climate in the western mining area is dry, with less rainfall. Therefore, high-intensity mining activities have severely impacted the local ecosystems (Reta et al. 2019). Statistics have shown that the coal mining industry produces 8 billion tons of groundwater every year in China, but only a quarter is well utilised. The loss of mine water resources is equivalent to 60% of the annual industrial and domestic water shortage (10 billion t) (Gu 2013; Si et al. 2010; Wang et al. 2017). Therefore, coordinating coal mining and water resource protection is one of the serious challenges of the western region. Gu (2015), Xie et al. (2015), and Yuan et al. (2018) presented several concepts for underground water and energy storage using underground coal mine openings. The proposed concepts, including underground water storage in the goaf, sewage treatment centers, and pumped storage power stations, provide promising ways to reuse the underground space and mine water and protect the environment and local ecologies. The underground water reservoir (UWR) technology (Fig. 1) has been used in the Shendong mining area. Thirty-five underground reservoirs with a total water storage of 25 million m^3 have been built; these could store more than 95% of the produced water from mining activities and surrounding industries, promoting its reuse in the area (Zhang et al. 2021).

During the construction of an underground reservoir, the main issues are the storage capacity of longwall goafs and the stability of the reservoir structures (Li et al. 2017a; Liu et al. 2019; Wang et al. 2020; Yao et al. 2020; Zhao et al.

✉ Cun Zhang
cumt-zc@cumtb.edu.cn

✉ Qingsheng Bai
qingsheng_bai@yahoo.com

1 Beijing Key Laboratory for Precise Mining of Intergrown Energy and Resources, China University of Mining and Technology, Beijing 100083, China

2 School of Energy and Mining Engineering, China University of Mining and Technology, Beijing 100083, China

3 State Key Laboratory of Groundwater Protection and Utilization by Coal Mining, Beijing 102209, China

4 Institute of Geotechnics, TU Bergakademie Freiberg, Gustav-Zeuner-Straße 1, 09599 Freiberg, Germany

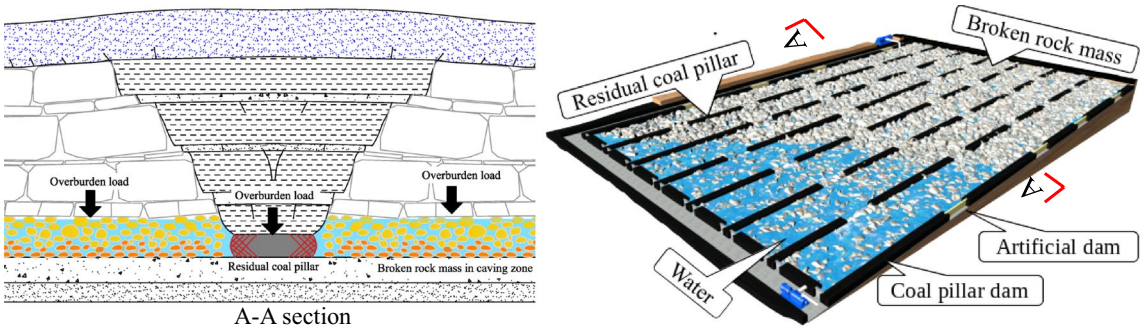

Fig. 1 Bearingstructure of underground reservoir in a mine

2019). Longwall goafs are the primary storage of underground reservoirs, and the porosity of the caving zone and its evolution law dominate the storage capacity (Wang et al. 2019; Zhang and Zhang 2019), as shown in Fig. 1. Therefore, porosity evolution in the caving zone during underground reservoir operation is an essential factor that affects water storage. The evolution of the caving zone's porosity is mainly divided into two stages, mining and underground reservoir operation (Li and Ju 2018; Li et al. 2019; Zhang et al. 2016, 2019). In the mining stage, the porosity of the caving zone (φ) gradually decreases with the overlying strata subsidence, and some models for calculating porosity were proposed (Bai et al. 2014, 2016; Yu et al. 2016; Zhang et al. 2016). However, these models need particle distribution parameters, which are usually challenging to obtain in the goaf (Karacan 2010; Fan and Liu 2017) proposed a method to calculate the porosity and permeability at each compaction stage of the caving zone without considering the broken rock mass dimension:

$$\frac{k}{k_0} = \left(\frac{V_0 - V_s / \left(1 - \frac{\sigma_z}{E_s}\right)}{V_0 - V_s} \right)^3 \tag{1}$$

where σ_z is the vertical stress, k_0 and k are the permeability before and after deformation, respectively. V_0 and V_s are the initial volume and deformation volume of the particle, respectively, and E_s is the secant modulus. The secant modulus gradually increases as the goaf compacts, which affects the porosity and permeability.

Permeability modes derived from experiments can consider many factors, for example, particle size and shape, particle strength, stress regime, and moisture effect (Chu et al. 2017; Jia et al. 2017; Li et al. 2017b; Zhang and Zhang 2019). However, these models cannot fully describe the permeability and porosity evolution in the goaf, which usually spatiotemporally evolves depending on the compaction process, stress environments, roof structures, and other factors. Numerical models have been developed to simulate the compaction process in the caving zone and the associated stress and permeability changes due to the limitations in the current theoretical and experimental models (e.g. Jin et al. 2010; Zhang et al. 2019). However, porosity evolution during compaction is usually ignored (Packham et al. 2011; Xia et al. 2016).

Numerical methods of physical and mechanical changes during caving zone compaction include microscopic laboratory-scale models using the discrete element method (DEM), and macro field-scale models using the finite element method (FEM). The main steps of DEM (e.g. PFC model) inversion are: (1) the broken rock mass can be simulated by particle clusters, which usually comprises several sub-particles. The clusters could further fail to simulate fragmentation of the rock blocks during the compaction process; (2) during the simulation process, the particle parameters and contact parameters can be modified to reproduce experimental results; and (3) the effect of particle breakage on the macroscopic behaviour of the assembly during the compaction process can then be realistically simulated (Manso et al. 2018; Sitharam and Vinod 2010; Zhang et al. 2020a). FEM models generally simulate the physical and mechanical behaviour of the goaf at the engineering scale. Experiment-derived models can be employed in these models (Bai et al. 2016; Zhang et al. 2016). However, porosity evolution in the caving zone during the mining stage cannot be used during the operation of underground reservoirs. The UWR is constructed after the longwall mining is completed, so that the caving zone will stay in a long-term immersion and loading environment (Fig. 1).

The effect of water infiltration on the deformation of an assembly of fragmented rocks is shown in Fig. 2. The pore structure of the assembly alters significantly during long-term water immersion. Ma et al. (2019) also found that the broken rock mass porosity increases during water flow due to mass loss, and erosion inhibits the growth of the fluid Forchheimer coefficient. Thus, broken rock mass movement affects the porosity distribution and seepage characteristics of the

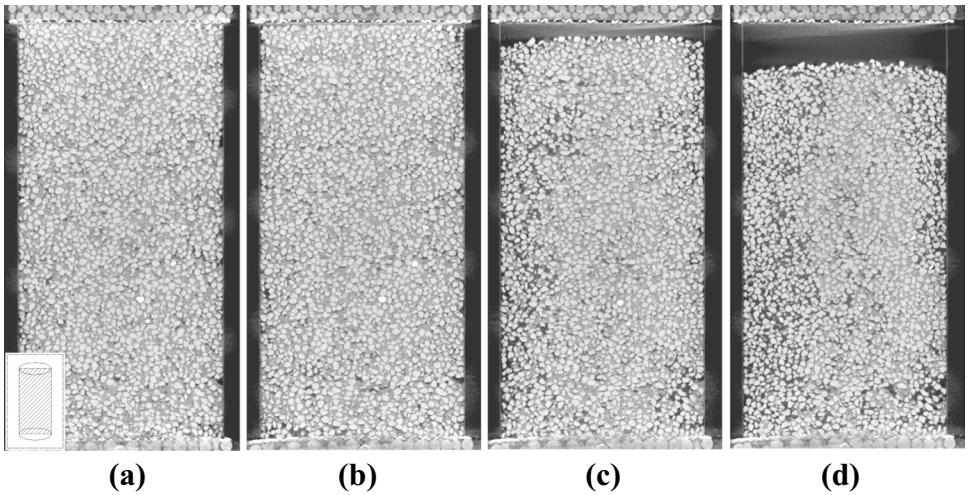

Fig. 2 Verticalsections of the four scans in the median plane of the sample (Nguyen etal. 2019), **a** the initial phase; **b** after applying a very low rate of0.05 cm/s; **c** after the sample was subject to a flow rate of 0.25 cm/s for 30min, and **d** after an additional 30 min loading with a flow rate of 0.45 cm/s

caving zone during the circulation storage and discharge in UWRs. Currently, research on the fluid-solid coupled of the broken rock mass usually focuses on particle soil loss. A new fluid-solid coupled numerical approach combined the DFM (dynamic fluid mesh) method with the DEM to simulate soil suffusion (Zhang et al. 2020b). This novel approach accounts for permeability and porosity changes due to soil skeleton deformation and suffusion. Nguyen and Indraratna (2020) used a similar method to address the complex processes of energy transformation during the internal erosion of soils subjected to fluid flow. This method can realise the fluid-solid coupled simulation of particles. However, the effect of the external stress and flow velocity on the simulation was rarely previously considered. In the underground reservoir, the complex and varying stress environment affects the porosity of the caving zone. Thus, this study establishes the coupled equation of mine water seepage and broken rock mass through theoretical analysis, which we then embedded in PFC3D and Python. Using the DEM-CFD coupled program, we investigated the effect of seepage on broken rock mass porosity under different stress states. The results clarify the porosity evolution of the caving zone in the process of mine water seepage.

Methodology

Hydraulic Forces Acting on Particles due to Fluid Flow

The hydraulic force exerted on the particles by the fluid (fluid-solid coupled interaction force) consists of the drag force and the force caused by the fluid pressure gradient:

$$\vec{f}_{fluid} = \vec{f}_{drag} + \frac{4}{3}\pi r^3 \vec{\nabla} p \tag{2}$$

where $\vec{f}_{fluid}$ is the total force exerted by the fluid on the particles, $\vec{f}_{drag}$ is the drag force applied by the fluid, r is the particle size, and $\vec{\nabla} p$ is the fluid pressure gradient.

The drag force exerted on the particles is individually determined based on the conditions of the fluid element. It should be noted that the hydraulic forces acting on particles are exerted on the centroid of the particle, and there is no torque effect. There are several methods to estimate the drag force (Wang and You 2011; Kafui et al. 2002) suggested that Felice (1994) can better present a smooth variation of drag force over porosity. This approach has been widely used (Nguyen and Indraratna 2020; Tao and Tao 2017). The drag force can be calculated using Eq. (3).

$$\vec{f}_{drag} = \frac{1}{2} C_d \rho_f \pi r^2 \left|\vec{u} - \vec{v}\right| \left(\vec{u} - \vec{v}\right) \phi^{-\chi} \tag{3}$$

where C_d is the drag coefficient, which can be calculated by Eq. (4), $\vec{u}$ is the particle velocity, $\vec{v}$ is the fluid velocity, ρ_f is the fluid density, and Φ is the porosity of the fluid element where the particle is located. χ is an empirical coefficient that considers local porosity. This correction coefficient makes the drag force suitable for high-porosity and low-porosity systems and supports a wide range of Reynolds numbers, as expressed in Eq. (5) (Felice 1994; Xu and Yu 1997).

$$C_d = \left(0.63 + \frac{4.8}{\sqrt{\mathrm{Re}_p}}\right)^2 \tag{4}$$

$$\chi = 3.7 - 0.65 \exp\left(-\frac{\left(1.5 - \log_{10}\mathrm{Re}_p\right)^2}{2}\right) \tag{5}$$

where R_e is the particle Reynolds number and can be expressed as:

$$\mathrm{Re}_p = \frac{2\rho_f r|\vec{u}-\vec{v}|}{\mu_f} \tag{6}$$

where μ_f is the fluid viscosity. If all particles are in the fluid, the equations describing the fluid-particle interaction are:

$$\frac{\partial \vec{u}}{\partial t} = \frac{\vec{f}_{mech} + \vec{f}_{fluid}}{m} + \vec{g} \tag{7}$$

$$\frac{\partial \vec{w}}{\partial t} = \frac{\vec{M}}{I} \tag{8}$$

where $\vec{f}_{mech}$ is the sum of the external mechanical forces acting on the particles, which includes the applied external forces and the contact forces, $\vec{g}$ is the gravity, $\vec{w}$ is the particle angular velocity, I is the moment of inertia, and $\vec{M}$ is the moment acting on the particles.

Solve Permeability and Fluid Velocity

Darcy's law can be used to describe the low Reynolds number for fluid in porous media. The upper limit of the Reynolds number corresponding to Darcy's law is between 1 and 10 (Diersch and Kolditz 2002). The velocity of the underground reservoir is low-speed flow. Therefore, Darcy's law can be expressed as:

$$\vec{v} = \frac{K}{\mu_f}\vec{\nabla} p \tag{9}$$

where K is the permeability and p is the fluid pressure. It is assumed that the compressibility of the fluid can be ignored. Therefore, the fluid pressure can be obtained according to the flow velocity through an implicit solution. The permeability coefficient is calculated based on the porosity of the porous media model. This study uses the Kozeny–Carman equation to calculate the permeability coefficient.

$$K(\phi) = \begin{cases} \dfrac{1}{180} \cdot \dfrac{\phi^3}{(1-\phi)^2}(2r)^2 & \phi \leqslant 0.7 \\ K(0.7) & \phi > 0.7 \end{cases} \tag{10}$$

To calculate the permeability coefficient and concurrently consider the condition of the reservoir, the upper limit of porosity is set to 0.7 (Itasca 2018). When the porosity exceeds 0.7, the permeability coefficient is constant. Equation (9) is the Darcy flow equation for a low Reynolds number. When the Reynolds number exceeds 10, Darcy flow is no longer applicable; the flow in porous media can then be described by the Forchheimer formula,

$$\vec{\nabla} p = \frac{\mu_f \vec{v}}{K} + \rho_f \beta \vec{v}^2 \tag{11}$$

where β is the non-Darcy flow factor. This study only focuses on Darcy flow.

Numerical Implementation

In this study, PFC3D was used to simulate the behaviour of the assembly of caved rocks, while computational fluid dynamics (CFD) solver was used to perform the fluid-solid coupled. In the coupling, the porosity and stress of each fluid element were calculated in PFC3D. The fluid velocity, fluid pressure, fluid pressure gradient, fluid density, and hydrodynamic viscosity coefficient in each fluid element were determined by the CFD solver (Fig. 3). The CFD module automatically exerts the fluid-particle interaction force for the PFC particles. Bidirectional coupling was achieved by updating the porosity and permeability in the fluid flow model and fluid velocity field in the CFD module. The steady-state flow field was automatically periodically updated at a particular step interval of the mechanical calculation. Synchronisation and exchange of data between the two solvers were performed via TCP socket communication using FISH or Python scripts.

The centre method was used to update the porosity of each fluid element due to its high accuracy. It is suitable for particles that are entirely immersed within the fluid element, so the fluid element and particle size need to be restricted. The generation of zero porosity in the fluid unit will lead to a singularity in the fluid governing equation (Eq. 3, the drag force will be infinite). Thus, the porosity of the fluid element was limited to more than 0.005. In using the complete particle volume to estimate porosity, the overlapped part is not accounted for, which causes the calculated porosity to be less than the actual value. Thus, to improve the reliability of the simulation, it is necessary to address the effect of scale factors R (fluid element size/particle diameter) and porosity on the numerical results. Several models with different scale factors and porosities were designed, as

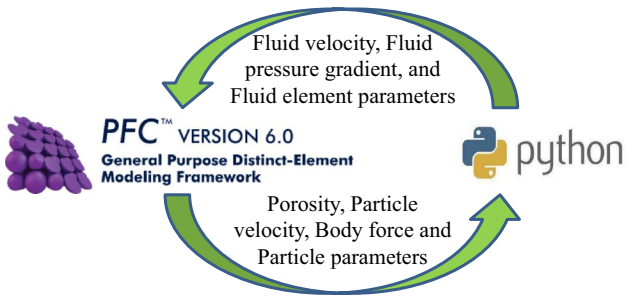

Fig. 3 CFD-DEMcoupling method by PFC3D and the CFD solver

shown in supplemental Fig. S-1; the simulation parameters are listed in Table 1.

The corresponding flow velocity simulation results are shown in Fig. S-2, accompanying the errors between the numerical results and theoretical calculation (Eq. 9). As can be seen from Fig. S-2, the flow velocity obtained by simulation increases exponentially with increased porosity, which is consistent with the theoretical calculation. However, as R decreases, the deviation between the simulation results and theoretical calculations gradually enlarges, which is due to increased porosity calculation error when R is small. This occurs mainly when one fluid element contains more particles. Porosity also plays a significant role in numerical accuracy. When the porosity is less than 0.25, the error rises to 14.1% even if the coefficient R reaches 20. Decreasing the porosity will increase the numerical error. A porosity of less than 0.1 would produce a deviation exceeding 100%. To limit the error to less than 10%, the porosity should range between 0.3 and 0.5, and the proportional coefficient R should exceed 3. When the coefficient R exceeds 10, the upper limit of the porosity can be increased. Figure S-3 shows the variance of porosity between the model generation process and the calculated value. It clearly shows that less porosity (<0.3) produces a larger error.

A porosity correction operation was introduced in the simulation to remove the porosity error. First, the average porosity of the CFD element was obtained by PFC3D calculation. Then, the porosity correction factor was calculated by the model porosity and average calculated porosity. Finally, the porosity used in the CFD solver was updated by the porosity correction factor. This operation can improve numerical accuracy, as shown in Fig. S-4. Consequently, the available ranges of R and porosity increased. The porosity should be within 0.2–0.4 to meet the error limitation (10%), for $R>2$. If $R>5$, the available porosity can range between and 0.1–0.5, covering most situations it may encounter in this study.

In addition to the flow velocity, the drag force error during simulation also affects the simulation results (Fig. S-5). According to the theoretical analysis, the drag force first decreased rapidly before increasing with porosity (Fig. 4) and diminished at porosity = 0.2. The simulation results shown in Fig. S-5 are consistent with the theoretical results. There should be no dramatic increase in the simulation results because porosity in an underground reservoir is generally above 0.1.

Like the flow velocity, as R increases, the numerical errors gradually decrease (Fig. S-5b). However, when the ratio coefficient R is 1, the numerical results are much larger than the theoretical values. Particle overlap is attributed to this large error because the calculated porosity approaches 0 under the condition of $R=1$, as shown in Fig. 4. In the

Table 1 Model parameters

Particle radius (m)	Emod (GPa)	Kratio	Fric	Inlet pressure (Pa)	Outlet pressure (Pa)	Fluid density (kg/m^3)	Fluid viscosity (Pa s)
0.025	25	2.0	0.5	500	0	1000	0.001

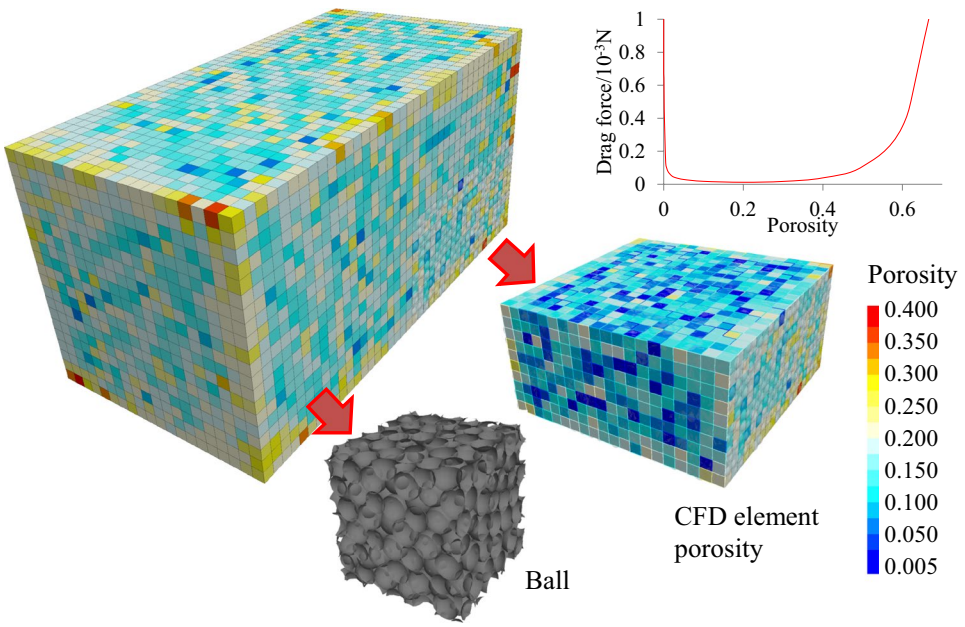

Fig. 4 Relationshipbetween porosity and drag force in low porosity assembly

process of fluid calculation, the overlapped part is not considered, resulting in the model's porosity tending to 0 or even a negative number. The porosity of the fluid element is limited to 0.005 to avoid the occurrence of zero porosity. According to the porosity evolution and drag force (Fig. 4), the drag force sharply increases to 1.3×10^{-4} N when the porosity tends to 0.005, which is much larger than when the porosity is 0.1 (1.76×10^{-5} N).

Porosity correction can remove the drag force error, as shown in Fig. S-5b. When $R>2$ and porosity is $\leq$0.2–0.4, the error can be limited to $\leq$10%. When $R>5$, the error can meet the requirements if the porosity is <0.5. In summary, to limit numerical errors, if the porosity ranges between 0.2 and 0.4, R should exceed 2. When $R>5$, the simulated porosity can be between 0.1 and 0.5.

Laboratory Calibration

Calibration of our model should be precise to accurately assess the storage capacity. Thus, we used the experimental results of Zhao et al. (2018) for laboratory calibration. The axial stresses in their tests were 10, 20, and 30 MPa, respectively. Four groups of particle sizes (3.8, 7.5, 12.5, and 17.5 mm) were assessed in their report. In our study, similar simulation parameters were used to simulate the stress-flow test with particle sizes of 3.8 and 12.5 mm. In each numerical case, the initial porosity was determined according to the measured permeability at 10 MPa. Then, a flow test of 20 and 30 MPa was used for calibration in our method. The simulated model and calibration results are shown in Fig. 5, the average errors (and normalized root mean square errors) for the test with particle sizes of 3.8 and 12.5 mm were 8.4% (6.2%) and 7.9% (6.7%), respectively, which clearly shows that the numerical and experimental results match well.

Fluid–Solid Coupled Simulation of the Caving Zone

In the error analysis, the vertical stress on the caving zone was not considered and the particle size of the broken rock mass was not consistent with that obtained from the experiment. In the caving zone, the contact stress between broken rocks significantly increases under the action of compaction stress, making it difficult for the broken rock mass to flow with the water. Therefore, this section further demonstrates particle migration and porosity evolution under different stress states during water seepage.

Model Setup

Water flow in the caving zone was simulated for this study. The vertical thickness of a goaf with a highly irregular shape and different granular broken rocks could reach 4–11 times the mining height (Karacan and Luxbacher 2010). The broken rocks were gradually compressed by the overburden load caused by mining (Fig. 1). Thus, the goaf broken rocks could be treated as a porous medium consisting of residual coal and broken rock blocks generated by caving, pilling, and recompression. To improve the calculation efficiency, the model had a cross-sectional size of 0.1×0.1 m and a length of 0.2 m. Impermeable walls were generated around the model. The flow rate at the inlet of the model was 0.2 m^3/s and the pressure at the outlet was set to 0. The rock block radius was divided into

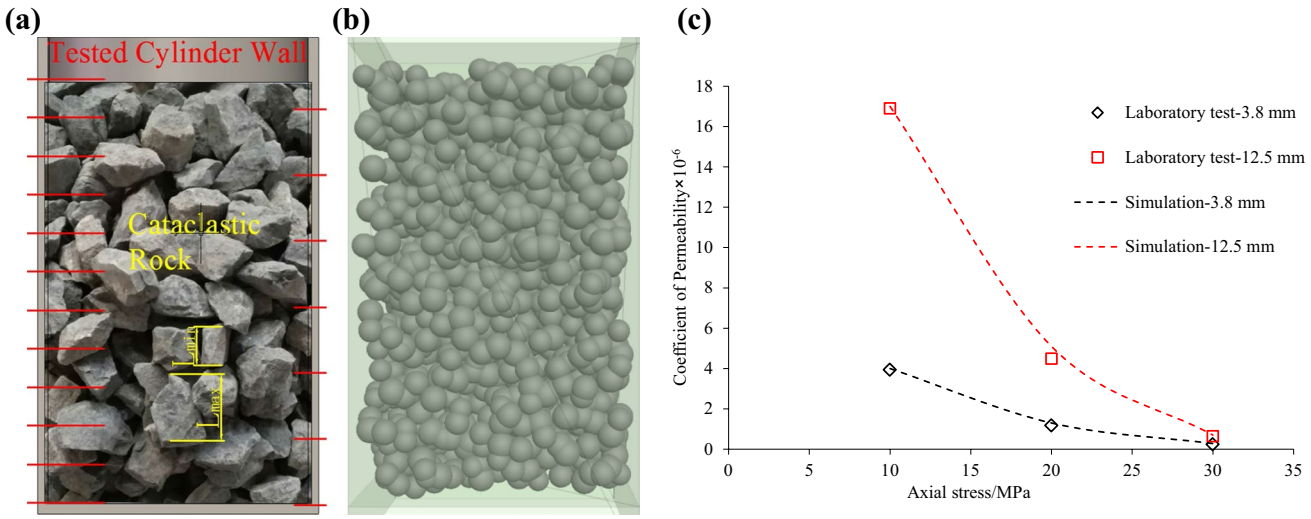

Fig. 5 Comparisonbetween laboratory test results and numerical simulation, **a** is laboratory testbroken rock, **b** is simulation model and **c** is comparison curves

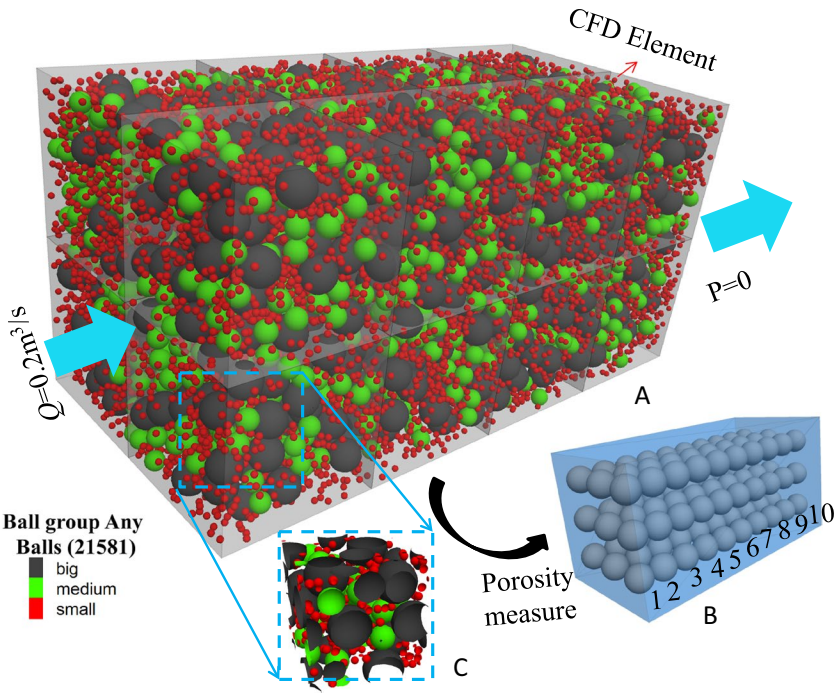

Fig. 6 Brokenrock mass model and porosity monitoring arrangement

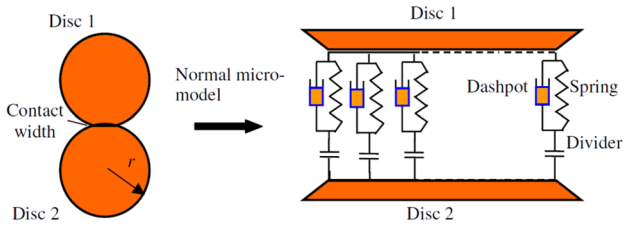

Fig. 7 RollingResistance Linear Model (modified after Ai et al. 2011; Wensrich and Katefeld 2012)

three groups based on the error analysis: 0.001, 0.003, and 0.005 m. The fluid element size was set to 0.05 m and the *R* of the three particle groups were 25, 8.3, and 5, respectively. The proportions of the three groups were 10%, 20%, and 70%, with 21,581 spheres. The initial porosity of the model was 0.6. When the overburden stress reached 1 MPa, the porosity remained constant (≈0.5), meeting the simulation requirement. The model is shown in Fig. 6.

To understand the influence of particle shape on the flow and mechanical behaviour, the rolling resistance linear contact model was used to describe the interaction between particles (Fig. 7); this model is described in more detail in Ai et al. (2011) and Wensrich and Katefeld (2012). The simulation parameters are listed in Table 2 (Shao et al. 2020). Ten groups (nine monitoring points in each group) were arranged inside the model to quantitatively analyse the porosity evolution at different positions of the model (Fig. 6B).

Table 2 Contact parameters of broken rock mass

Elastic modulus (GPa)	Stiffness proportional coefficient	Friction coefficient	Rolling friction coefficient
25.00	2.0	0.49	0.9

Results and Discussions

Displacement of the Rock Blocks

Simulations were conducted under axial stresses of 1, 2, 3, 4, 5, 10, and 15 MPa to study the influence of overburden stress on the displacement of rock blocks. Smaller particles usually move with greater velocity. We assumed that the model had stabilised when the average displacement increase of small particles was less than 10^{-5} m in 10,000-time steps. The time steps required to reach equilibrium for each scenario are shown in Table 3. Figure 8 proves the particle displacement after the model stabilised.

The particle displacement depends on the stress conditions even under the same flow velocity. When the overburden stress was small (1 and 2 MPa), particles near the water inlet side had larger displacements. As the stress increased, particle migration near the inlet was immensely reduced. For models with less overburden pressure (1 and 2 MPa), the roof was lifted because the flow produced higher fluid stress than the overburden pressure (Fig. 9),

Table 3 Displacement of particles after stabilization under different overburden stress

Stress /MPa		1	2	3	4	5	10	15
Average displacement/mm	Big	20.91	8.99	4.98	3.69	2.82	1.23	0.80
	Medium	23.49	10.36	5.84	4.51	3.61	1.96	1.51
	Small	33.76	16.91	10.69	8.73	7.59	5.51	4.93
Maximum displacement/mm	Big	54.26	33.66	21.96	19.98	17.96	14.71	12.60
	Medium	67.41	36.50	28.41	28.73	28.47	22.72	20.88
	Small	168.17	135.10	132.68	134.44	136.20	84.79	66.91
Time steps = 1×10^{-7} s		2.1×10^{6}	5.3×10^{5}	2.0×10^{5}	1.9×10^{5}	1.1×10^{5}	1.0×10^{5}	0.9×10^{5}

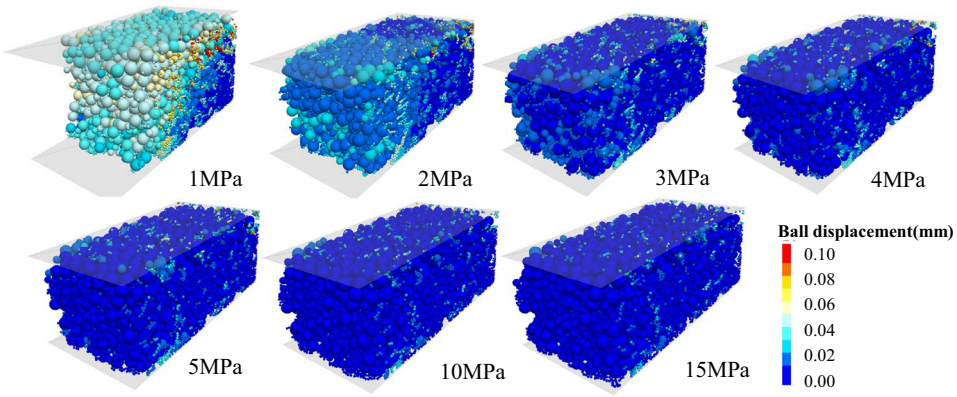

Fig. 8 Migrationof broken rock mass under different stress conditions

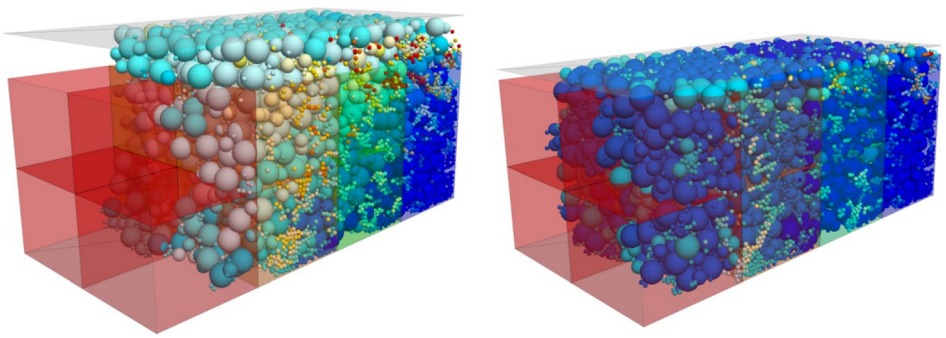

(a)1MPa **(b)**2MPa

Fig. 9 Roofuplift under low axial stress

which is consistent with the current study of the surface uplift caused by the water level recovery (mine flooding) in abandoned mines(Dudek et al. 2020; Zhao and Konietzky 2020).

The equilibrium time required for 1 MPa to reach equilibrium is much longer than that for the other scenarios. Under the stress condition of 1–4 MPa, small particles did not reach equilibrium when operated for 80,000 steps (Fig. 10). When the stress exceeded 5 MPa, the particle displacement roughly remained after 50,000 steps, indicating that overburden stress also affects the particle balance time (Table 3).

As the overburden stress increased, the average displacement of the assembly decreased exponentially, Fig. 11a. At the same stress level, large particles witnessed similar displacement evolution as that of the medium particle group, but much less than the small particle group because the acceleration of small particles in the same flow field was greater than that of larger particles. Another reason was those small particles were generally located in spaces surrounded by larger particles, which usually have lower stress, as can be seen in Fig. 6. However, all the curves in Fig. 11a show similar variation with stress, which indicates that particle size did not affect the stress dependence of particle displacement. In Fig. 11b, the maximum displacement of small particles varies only slightly under the stress of 5 MPa, while the maximum displacement of broken rock masses

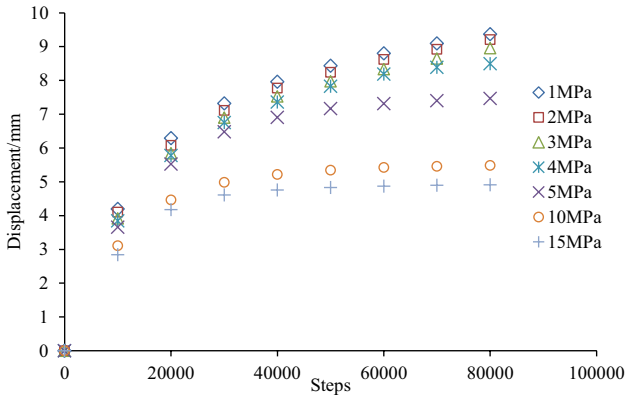

Fig. 10 Displacementevolution of small particles under different stress conditions

with large and medium particles decreased exponentially (Fig. 11b), confirming that small particles in the assembly are not the main load-bearing body of stress.

Porosity Evolution

The migration of rock blocks directly affects the porosity evolution of the model, which, in turn, also affects the permeability and water storage capacity of the caving zone. Fig. S-6 shows the average porosity of each monitoring layer of the model under different stress states.

The evolution of the porosity depends on both the location and overburden stress. In the first layer (close to the inlet), the porosity gradually increased and remained constant, regardless of the stress. The porosity of the last two layers (near the outlet) monotonously decreased. When the overburden stress was 1 MPa, the porosity of each layer fluctuated. This trend was more significant in layers 3–8. The reason for this is believed to be the uplift of the top boundary. When the overburden stress was increased beyond 1 MPa, the porosity of layers 2–8 were not significantly affected (0.4–0.5), but when the overburden stress was exceedingly high, the first layer showed a marginal increase in porosity, that is 0.047 at 10 MPa and 0.023 at 15 MPa. The porosity increase in the first layer was much greater within the range of 0.54–0.14 as the overburden stress increased from 1 to 5 MPa (Fig. S-6), which is mainly because only small particles migrate under high-stress conditions, with little effect on the porosity. Moreover, an increase in overburden stress further enhances the migration resistance of rock blocks and reduces the pore space between larger particles. The former dominates the migration of large particles, while the latter controls the migration of small particles. Note that porosity changes are closely related between two adjacent layers. With the rapid porosity increase in the previous layer, other layers would simultaneously witness porosity decreasing, indicating particle migration.

Notably, the size of the broken rock mass in the caving zone was much greater than the simulated cases in this study. The overburden stress was roughly 5 MPa (at a buried depth > 200 m). Therefore, the drag force generated by fluid flow in the underground reservoir cannot move the large particles. The migration of small rock blocks (including dust) dominates the porosity changes. Further, the increase in the water inlet porosity can be obtained from the simulation in which the porosity was gradually reduced near the outlet. With so many small particles in the caving zone, the porosity near the outlet was greatly reduced, obstructing the water outlet.

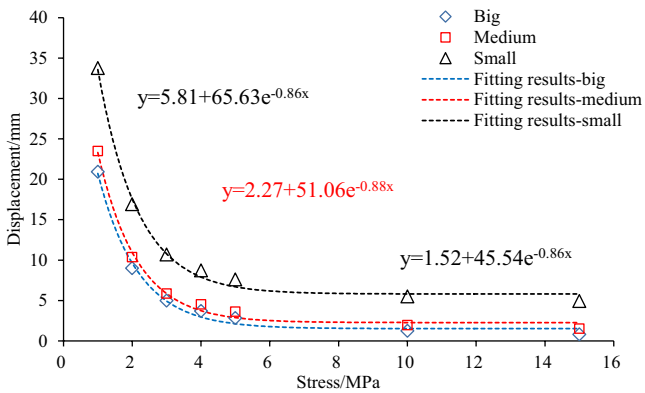

(a) Average displacement

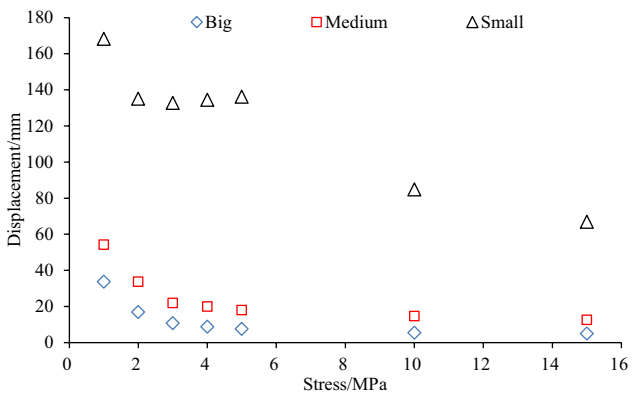

(b) maximum displacement

Fig. 11 Displacementand stress evolution curves of broken rock mass with different particle sizes

Discussions

This study used a numerical method to study the migration and pore evolution of broken rock masses during the storage and discharge of underground reservoirs. The influence of overlying stress and particle size on porosity changes was investigated. Numerical results showed that the proposed method could mimic fluid-solid coupling in the caving zone and reproduced well the migration of small particles observed in laboratory experiments. For example, a series of seepage-induced particle erosion experiments were conducted by Ma et al. (2019), who found that the porosity of the broken rock mass was increased by the mass loss. Further, large particle rearrangements in the early stages dominate the sharp increase in porosity, and small particle losses induces a slight decrease in porosity. Moreover, the porosity of the model under different overburden stresses agreed well with the experimental results obtained by Li et al. (2019) and Zhang et al. (2019). The effects of porosity, particle size, and water pressure (flow rate) on the drag force and the simulation results were consistent with the theoretical model (Dong et al. 2014; Kaur and Alam 2016; Rubinstein et al. 2016; Wang et al. 2011), as shown in Fig. S-7. The average errors (and normalized root mean square errors) for the simulation with particle sizes of 0.005 m and a flow rate of 0.2 $m^{3/}$s were 5.1% (0.2%) and 7.9% (0.1%), respectively. Earlier, we compared our simulation results with the laboratory flow test of broken rock mass under different loading stresses by Zhao et al. (2018). The simulation results matched the experimental results. However, compared with other experiments, our simulation results were not exceptionally good, mainly because we did not consider the re-crushing of the broken rock mass during loading. It should be possible to solve this problem by using a parallel bond model to generate particle clusters (Zhang et al. 2020a, b), enhancing the accuracy of the simulation.

Due to the high calculation consumption, a small-scale model with large particles was used to simulate particle migration and the associated porosity changes. The model also simplified field conditions, for example, neglecting the water pressure and flow rate variation, particle size effect, and mass loss during discharge; therefore, the numerical results cannot be applied to field applications. Thus, our model should be upscaled, considering critical factors such as preferential flow; the concept will be useful in assessing the behaviour and storage capacity of goaf material in different flow fields. Residual coal pillars in underground reservoirs will also affect the water seepage law (Fig. 1) and should be considered in further studies. Besides, only the migration law of water in the caving zone was simulated. After longwall mining, the overlying strata form caving, fractured, and bedding zones, ordered from bottom to top. The caving zone has the largest storage volume, and the fractured zone contains the majority of the water-conducted channels (Palchik 2003; Zhang et al. 2017, 2018). Moreover, the fractured zone can also provide storage space for an underground reservoir and the water flow in the fractured zone will also carry particles (Yang et al. 2021; Zhang et al. 2021). Thus, the water flow in the fracture zone should also be considered in the CFD-DEM coupled simulation of an underground goaf reservoir.

At present, the most important issue for field-scale simulation is to determine the size of the broken rock mass in the caving zone. For several reasons such as difficulty in entering the goaf, the measurement of the size distribution of the broken coal and rock mass is very challenging. Pappas and Mark (1993) and Singh and Singh (2011) have reported the gradation of broken rock mass in the goaf. Photographs of the actual mine goaf were digitised to obtain approximate particle size gradations of the goaf material. Figure 12 shows the estimated gradation curves for each goaf site photographed and indicates that the goaf gradation for the three sites may fall within a narrow range. However, in these two studies, only the bottom of the caving zone

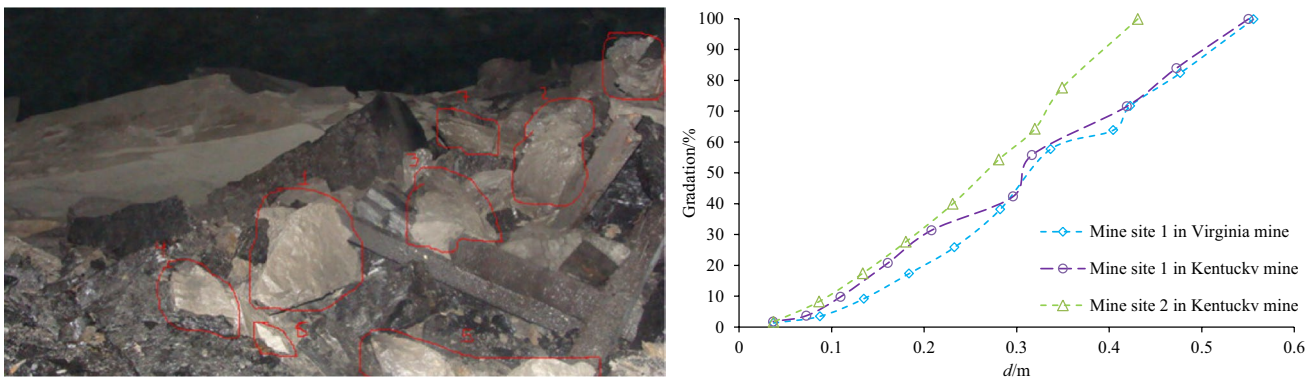

Fig. 12 Gobmaterials photographed and approximate particle size gradations of gob material

could be photographed, where the caved rocks are usually more finely fragmented than in the upper part of the goaf. Thus, further studies of particle size distributions in the goaf remains a critical need. Moreover, the low computational efficiency for field-scale models is also a challenge to be solved. Taking the Shangwan coal mine as an example, the model dimensions need to be at least 300 × 300 × 10 m. According to the goaf grading distribution given by Pappas and Mark (1993), a reduced scale model (30 × 30 × 1 m) with a porosity of 0.4 is shown in Fig. 13. There are 246,512 balls in this model; the number of balls in the full-scale model would be ≈ 250 million, beyond the ability of common computers. However, the proposed method demonstrates a promising way to study the fluid-solid coupled of water seepage in a goaf reservoir. Future work will focus on more realistic field conditions, as shown in Fig. 13.

Conclusions

In this study, we constructed a fluid-solid coupled model to simulate the migration and pore evolution of broken rock masses during the storage and discharge of underground reservoirs. This model mainly describes the force between the fluid and particles in the form of fluid stress (drag force + buoyancy). The Kozeny–Carman equation was used to calculate the permeability based on the porosity of the assembly. The theoretical model was embedded in the PFC3D code and combined with the Python flow solver to realise the fluid-solid coupled simulation. The influence of particle size and fluid element size on the error of the simulation results was analysed. Then, we investigated the effect of seepage on broken rock mass porosity under different stress states. The proposed method is a promising method for assessing the behaviour and storage capacity of goaf material under actual conditions. The major findings were:

(1) The numerical results showed that the error between the pre-set porosity and the calculated porosity plays a significant role in the simulation results. Introducing porosity correction is a feasible way to weaken the effects of this error. When the porosity is set between 0.2 and 0.4, the coefficient R should be larger than 2. When the simulated porosity is expanded between 0.1 and 0.5, the coefficient R can be above 5. With this correction, the simulation errors can be reduced to less than 10%.
(2) Simulations with various particle sizes and stress regimes show that when the overburden stress is relatively small (1 and 2 MPa in this study), the rock particles will migrate significantly during the seepage process, causing the roof to rise. As the stress increases,

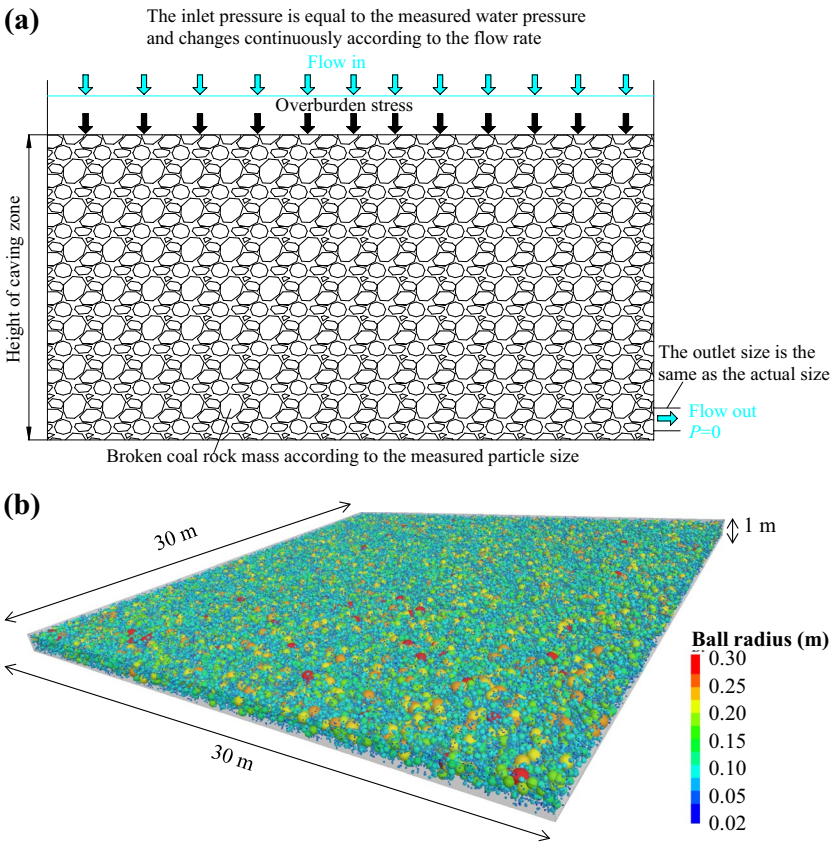

Fig. 13 Flow-solidcoupling model of caving zone under engineering scale conditions, **a** is the simulationscheme and **b** is the reduced scale simulation model

the average displacement of the broken rock particle decreases exponentially. Small particles always move more than large particles. Under high-stress conditions (10 and 15 MPa), only small rock particles, which usually reside in pore spaces, will experience significant displacement.

(3) The movement of particles in the broken rock model directly affects the porosity of the model. Under high-stress conditions (10 and 15 MPa), large particles become the main bearing structure. Therefore, the migration of small particles dominates porosity changes, having a limited effect on water seepage. If low overburden stress (1–5 MPa) is applied, the model's porosity gradually increases from the outside to the inside according to the particle migration.

Supplementary Information The online version contains supplementary material available at https://doi.org/10.1007/s10230-021-00826-7.

Acknowledgements Financial support for this study was provided by the Beijing Municipal Natural Science Foundation (8212032), the National Natural Science Foundation of China (U1910206, 52104155, 51874312), the Open Fund of State Key Laboratory of Water Resources Protection and Utilization in Coal Mining (WPUKFJJ2019-15), and the Fundamental Research Funds for the Central Universities (2021YQNY11). We also thank the anonymous reviewers for their constructive comments and suggestions on the draft manuscript.

References

Ai J, Chen JF, Rotter JM, Ooi JY (2011) Assessment of rolling resistance models in discrete element simulations. Powder Technol 206(3):269–282

Bai QS, Tu SH, Chen M, Zhang C (2016) Numerical modeling of coal wall spall in a longwall face. Int J Rock Mech Min 88:242–253

Bai QS, Tu SH, Zhang XG, Zhang C, Yuan Y (2014) Numerical modeling on brittle failure of coal wall in longwall face—a case study. Arab J Geosci 7(12):5067–5080

Chu T, Yu M, Jiang D (2017) Experimental investigation on the permeability evolution of compacted broken coal. Transport Porous Med 116(2):847–868

Diersch HJG, Kolditz O (2002) Variable-density flow and transport in porous media: approaches and challenges. Adv Water Resour 25(8):899–944

Dong S, Zheng L, Zhang X, Lin P (2014) Improved drag force model and its application in simulating nanofluid flow. Microfluid Nanofluid 17(2):253–261

Dudek M, Tajdus K, Misa R, Sroka A (2020) Predicting of land surface uplift caused by the flooding of underground coal mines—a case study. Int J Rock Mech Min 132:104377

Fan L, Liu S (2017) A conceptual model to characterize and model compaction behavior and permeability evolution of broken rock mass in coal mine gobs. Int J Coal Geol 172:60–70

Felice RD (1994) The voidage function for fluid–particle interaction systems. Int J Multiphas Flow 20(1):153–159

Gu D (2015) Theory framework and technological system of coal mine underground reservoir. J China Coal Soc 40(2):239–246 (**In Chinese**)

Gu D (2013) Water resource and surface ecology protection technology of modern coal mining in China's energy "Golden Triangle". Eng Sci 15(4):102–107

Itasca (2018) PFC (Particle Flow Code) Version 6. Itasca Consulting Group Inc., Minneapolis

Jia Y, Xu B, Chi S, Xiang B, Zhou Y (2017) Research on the particle breakage of rockfill materials during triaxial tests. Int J Geomech 17(10):4017085

Jin LZ, Yao W, Zhang J (2010) CFD simulation of gas seepage regularity in goaf. J China Coal Soc 35(9):1476–1480

Kafui KD, Thornton C, Adams MJ (2002) Discrete particle-continuum fluid modelling of gas–solid fluidised beds. Chem Eng Sci 57(13):2395–2410

Karacan CO (2010) Prediction of porosity and permeability of caved zone in longwall gobs. Transport Porous Med 82(2):413–439

Kaur J, Alam MA (2016) Study on estimation of hydraulic conductivity of porous media using drag force model. Int J Innov Res Sci Eng Technol 2(3):853–859

Li B, Ju F (2018) An experimental investigation into the compaction characteristic of granulated gangue backfilling materials modified with binders. Environ Earth Sci 77(7):284

Li B, Liang Y, Zhang L, Zou Q (2019) Experimental investigation on compaction characteristics and permeability evolution of broken coal. Int J Rock Mech Min 118:63–76

Li Q, Ju J, Cao Z, Gao F, Li J (2017) Suitability evaluation of underground reservoir technology based on the discriminant of the height of water conduction fracture zone. J China Coal Soc 42(8):2116–2124 (**In Chinese**)

Li M, Zhang J, Zhou N, Huang Y (2017b) Effect of particle size on the energy evolution of crushed waste rock in coal mines. Rock Mech Rock Eng 50(5):1347–1354

Liu Q, Sun Y, Xu Z, Jiang S, Zhang P, Yang B (2019) Assessment of abandoned coal mines as urban reservoirs. Mine Water Environ 38(2):215–225

Ma D, Duan H, Li X, Li Z, Zhou Z, Li T (2019) Effects of seepage-induced erosion on nonlinear hydraulic properties of broken red sandstones. Tunn Undergr Sp Tech 91:102993

Manso J, Marcelino J, Caldeira L (2018) Crushing and oedometer compression of rockfill using DEM. Comput Geotech 101:11–22

Nguyen CD, Benahmed N, Ando E, Sibille L, Philippe P (2019) Experimental investigation of microstructural changes in soils eroded by suffusion using x-ray tomography. Acta Geotech 14(3):749–765

Nguyen TT, Indraratna B (2020) The energy transformation of internal erosion based on fluid-particle coupling. Comput Geotech 121:103475

Pappas DM, Mark C (1993) Behavior of simulated longwall gob material. US Dept of the Interior, Washington

Palchik V (2003) Formation of fractured zones in overburden due to longwall mining. Environ Geol 44:28–38

Packham R, Cinar Y, Moreby R (2011) Simulation of an enhanced gas recovery field trial for coal mine gas management. Int J Coal Geol 85(3):247–256

Reta GL, Dong X, Su B, Hu X, Bo H, Wan H (2019) The influence of large scale phosphate mining on the water quality of the Huangbaihe River basin in China: dominant pollutants and spatial distributions. Mine Water Environ 38(2):366–377

Rubinstein GJ, Derksen JJ, Sundaresan S (2016) Lattice Boltzmann simulations of low-Reynolds-number flow past fluidized spheres: effect of Stokes number on drag force. J Fluid Mech 788:576–601

Shao XQ, Chi SC, Tao Y, Zhou XX (2020) DEM simulation of the size effect on the wetting deformation of rockfill materials based on single-particle crushing tests. Comput Geotech 123:103429

Si H, Bi H, Li X, Yang C (2010) Environmental evaluation for sustainable development of coal mining in Qijiang, western China. Int J Coal Geol 81(3):163–168

Singh GSP, Singh UK (2011) Assessment of goaf characteristics and compaction in longwall caving. Min Technol 120(4):222–232
Sitharam TG, Vinod JS (2010) Evaluation of shear modulus and damping ratio of granular materials using discrete element approach. Geotech Geol Eng 28(5):591–601
Tao J, Tao H (2017) Factors affecting piping erosion resistance: revisited with a numerical modeling approach. Int J Geomech 17(11):4017097
Wang T, Yang C, Li J, Li J, Ma H (2017) Failure analysis of overhanging blocks in the walls of a gas storage salt cavern: a case study. Rock Mech Rock Eng 50(1):125–137
Wang BF, Sun KM, Liang B, Sun WJ (2019) Development and application of an experimental device for measuring storage coefficient in a coal mine underground reservoir. Arch Min Sci 64(4):655–670
Wang H, Zhang B, Yu X, Xu N, Ye J (2020) Long-term stability and deformation behaviour of anhydrite mine-out for crude oil storage. Rock Mech Rock Eng 53(4):1719–1735
Wang X, You C (2011) Evaluation of drag force on a nonuniform particle distribution with a meshless method. Particuology 9(3):288–297
Wang X, Liu K, You C (2011) Drag force model corrections based on nonuniform particle distributions in multi-particle systems. Powder Technol 209:112–118
Wensrich CM, Katterfeld A (2012) Rolling friction as a technique for modelling particle shape in DEM. Powder Technol 217:409–417
Xia T, Zhou F, Wang X, Zhang Y, Li Y, Kang J (2016) Controlling factors of symbiotic disaster between coal gas and spontaneous combustion in longwall mining gobs. Fuel 182:886–896
Xie HP, Hou ZM, Gao F, Zhou L, Gao YN (2015) A new technology of pumped-storage power in underground coal mine: principles, present situation and future. J China Coal Soc 40(5):965–972. [in Chinese]
Xu BH, Yu AB (1997) Numerical simulation of the gas-solid flow in a fluidized bed by combining discrete particle method with computational fluid dynamics. Chem Eng Sci 52(16):2785–2809
Yao Q, Tang C, Xia Z, Liu X, Zhu L, Chong Z, Hui X (2020) Mechanisms of failure in coal samples from underground water reservoir. Eng Geol 267:105494
Yu B, Chen Z, Ding Q, Wang L (2016) Non-Darcy flow seepage characteristics of saturated broken rocks under compression with lateral constraint. Int J Min Sci Techno 26(6):1145–1151
Yuan L, Jiang Y, Wang K, Zhao Y, Hao X, Xu C (2018) Precision exploitation and utilization of closed/abandoned mine resources in China. J China Coal Soc 43(1):14–20 (**In Chinese**)
Yang B, Yang T, Hu J (2021) Numerical simulation of non-darcy flow caused by cross-fracture water inrush, considering particle loss. Mine Water Environ 40(2):1–13
Zhang C, Tu S, Zhang L (2017) Analysis of broken coal permeability evolution under cyclic loading and unloading conditions by the model based on the hertz contact deformation principle. Transport Porous Med 119(3):739–754
Zhang C, Zhang L, Tu S, Hao D, Teng T (2018) Experimental and numerical study of the influence of gas pressure on gas permeability in pressure relief gas drainage. Transport Porous Med 124(3):995–1015
Zhang C, Zhang L (2019) Permeability characteristics of broken coal and rock under cyclic loading and unloading. Nat Resour Res 28(3):1055–1069
Zhang C, Tu S, Zhao Y (2019) Compaction characteristics of the caving zone in a longwall goaf: a review. Environ Earth Sci 78(1):27
Zhang C, Tu S, Zhang L, Bai Q, Yuan Yong, Wang F (2016) A methodology for determining the evolution law of gob permeability and its distributions in longwall coal mines. J Geophys Eng 13(2):181–193
Zhang C, Wang F, Bai Q (2021) Underground space utilization of coalmines in China: a review of underground water reservoir construction. Tunn Undergr Sp Tech 107:103657
Zhang C, Liu J, Zhao Y, Han P, Zhang L (2020a) Numerical simulation of broken coal strength influence on compaction characteristics in goaf. Nat Resour Res 29(4):1–17
Zhang F, Wang T, Liu F, Peng M, Furtney J, Zhang L (2020b) Modeling of fluid-particle interaction by coupling the discrete element method with a dynamic fluid mesh: implications to suffusion in gap-graded soils. Comput Geotech 124:103617
Zhao J, Konietzky H (2020) Numerical analysis and prediction of ground surface movement induced by coal mining and subsequent groundwater flooding. Int J Coal Geol 229:103565
Zhao J, Yin L, Guo W (2018) Stress–seepage coupling of cataclastic rock masses based on digital image technologies. Rock Mech Rock Eng 51(8):2355–2372
Zhao L, Sun C, Yan P, Zhang Q, Wang S, Luo S, Mao Y (2019) Dynamic changes of nitrogen and dissolved organic matter during the transport of mine water in a coal mine underground reservoir: column experiments. J Contam Hydrol 223:103473

Publisher's Note Springer Nature remains neutral with regard to jurisdictional claims in published maps and institutional affiliations.